IOP Publishing Nanotechnology
Nanotechnology 34 (2023) 055704 (8pp) https://doi.org/10.1088/1361-6528/ac9fdc

Janus (Mo/β-Mo_2C)@C heterostructure as an efficient electrocatalyst for the hydrogen evolution reaction in acidic and alkaline media

Weiwei Zhu[1,2,*], Zhongya Jiang[1], Xiang Peng[3], Zhaorong Li[2], Abebe Reda Woldu[2,4,*], Fushen Lu[2], Yiwen Fang[2], Paul K Chu[5] and Liangsheng Hu[2]

[1] Department of Mechanical Engineering, Shantou University, Guangdong, 515063, People's Republic of China
[2] Department of Chemistry and Key Laboratory for Preparation and Application of Ordered Structural Materials of Guangdong Province, Shantou University, Guangdong, 515063, People's Republic of China
[3] Hubei Key Laboratory of Plasma Chemistry and Advanced Materials, Hubei Engineering Technology Research Center of Optoelectronic and New Energy Materials, Wuhan Institute of Technology, Wuhan, 430205, People's Republic of China
[4] Department of Chemistry, College of Science, Bahir Dar University, Bahir Dar 79, Ethiopia
[5] Department of Physics, Department of Materials Science and Engineering, and Department of Biomedical Engineering, City University of Hong Kong, Tat Chee Avenue, Kowloon, Hong Kong, People's Republic of China

E-mail: wwzhu@stu.edu.cn and abebe.reda@yahoo.com

Received 29 June 2022, revised 2 November 2022
Accepted for publication 3 November 2022
Published 17 November 2022

Abstract

To explore low-cost, high-efficiency, and noble-metal-free catalysts for electrocatalytic water splitting in both acidic and alkaline media, the metal-metal carbide Janus hierarchical structure comprising Mo and β-Mo_2C embedded on a carbon layer (Mo/β-Mo_2C)@C is synthesized by a hydrothermal reaction and subsequent low-temperature magnesium thermic process. Systematic characterization by XRD, XPS, Raman scattering, and SEM/TEM reveals the successful formation of metallic Mo and β-Mo_2C nanoparticles. The synthesized (Mo/β-Mo_2C)@C has a large specific surface area and boasts highly efficient hydrogen evolution reaction activity including low overpotentials of 152 and 171 mV at a current density of 10 mA cm^{-2} and small Tafel slopes of 51.7 and 63.5 mV dec^{-1} in acidic and alkaline media, respectively. In addition, the catalyst shows outstanding stability for 48 h in both acidic and alkaline media. The excellent catalytic activity originates from more active sites and greater electron conductivity bestowed by the carbon layer, which also improves the long-term stability in both acidic and alkaline solutions.

Supplementary material for this article is available online

Keywords: janus (Mo/β-Mo_2C)@C heterojunction, electrocatalyst, hydrogen evolution reaction, magnesium thermic reaction

(Some figures may appear in colour only in the online journal)

* Authors to whom any correspondence should be addressed.

1. Introduction

The great challenge nowadays is to reduce the emission of greenhouse gases such as carbon dioxide (CO_2) [1–5] and clean hydrogen energy has emerged to be a potential alternative to fossil fuels [6–9]. The hydrogen evolution reaction (HER) in water splitting is the ideal way to produce clean hydrogen but requires efficient and economical electrocatalysts [10, 11]. So far, noble metals such as platinum (Pt) exhibit the best electrocatalytic HER activity with low overpotentials due to its suitable binding ability with hydrogen [12–15]. However, the high cost and scarcity of precious metals hamper wider commercial adoption and it is imperative to identify noble metal-free and low-cost electrocatalysts for efficient water splitting. To date, several Earth-abundant electrocatalysts have been designed for HER in acidic solutions [10, 16–20]. However, despite recent advances, it is still challenging to fabricate nanocatalysts for HER in both acidic and alkaline media on a large scale.

Molybdenum-based materials especially molybdenum carbide (Mo_2C) have attracted a lot of attention for HER due to the diverse electronic state and tunable phases [21, 22]. Moreover, the Fermi level of Mo_2C is similar to that of Pt resulting in high stability and environmentally friendliness [23–25]. However, Mo_2C has large electrical resistance which can partially be overcome by producing Mo_2C on conductive substrates [26, 27]. For instance, Wang *et al* [27] have prepared Mo_2C on carbon sheets showing an overpotential of 178 mV for a current density of 10 mA cm^{-2} in alkaline HER. Integration of metal and metal carbide heterojunctions further boosts the HER performance in a wide pH range. For example, Ni atomically dispersed on β-Mo_2C exhibits superior HER catalytic activity in a wide pH range [28]. To further enhance the catalytic activity as well as long-term stability in HER, integrating a metal-metal carbide heterojunction with graphene or carbon nanofibers is a promising approach [29–33]. Carbon nanomaterials provide a large surface area and excellent conductivity to facilitate electron transport [16, 34, 35].

Herein, a facile approach is described to synthesize Janus Mo/β-Mo_2C encapsulated with carbon layers ((Mo/β-Mo_2C)@C). The heterojunction electrocatalyst is prepared by a hydrothermal reaction and subsequent low-temperature magnesium thermic reaction of MoO_x-ethylenediamine (MoO_x-EDA). During the thermic process, Mo and β-Mo_2C are produced from the MoO_x-EDA precursor and the mass ratio of MoO_x-EDA and magnesium (Mg) affects the concentration of metallic molybdenum (Mo) in the materials. The thermic reaction decomposes $NaHCO_3$ into CO_2 that immediately reacts with Mg to release carbon and consequently, the Mo/β-Mo_2C heterostructure is encapsulated by carbon to increase the surface area, conductivity, and electron transfer. The (Mo/β-Mo_2C)@C heterojunction shows excellent HER characteristics in both acidic and alkaline media due to more abundant reactive sites and higher electrical conductivity rendered by carbon which also stabilizes the catalyst by preventing corrosion and oxidation during long-term electrolysis. This study reveals the large potential of the design and materials for high-performance HER in acidic and alkaline media.

2. Experimental

2.1. Synthesis of MoO_x-EDA inorganic-organic hybrids

MoO_x-EDA was prepared according to the technique for WO_3-EDA with modification [36]. In brief, 300 mg of molybdic acid ($MoO_3 \cdot H_2O$) powders were dispersed in 30 ml of ethylenediamine (EDA) in a beaker and stirred for 1 h before transferring to a 50 ml Teflon-lined stainless-steel autoclave. The reaction proceeded at 180 °C for 3 h and the white products formed were collected and rinsed with ethanol and deionized water.

The (Mo/β-Mo_2C)@C nanorods were produced by a low-temperature magnesiothermic reduction (MTR) [16, 37, 38]. Typically, 300 mg of sodium bicarbonate ($NaHCO_3$) and 100 mg of MoO_x-EDA were mixed, and then 25, 50, and 100 mg of magnesium powders were introduced to the mixture and transferred to a half-sealed stainless steel can placed at the center of a quartz tube in a tube furnace. The can was heated at 650 °C, 700 °C, and 750 °C (5 °C min^{-1}) for 3 h and then cooled to room temperature under an argon flow (99.99%). The product was rinsed with an excess amount of 3 M HCl to remove the residual Mg and by-product (MgO), washed with deionized water and ethanol 5 times to remove HCl, and vacuum dried at 80 °C overnight. The sample was denoted as (Mo/β-Mo_2C)@C. For comparison, MoO_x-EDA powders were calcined in H_2/Ar at 750 °C (5 °C min^{-1}) for 3 h directly to produce Mo/β-Mo_2C.

2.2. Characterization

The morphologies of the as-prepared samples were analyzed by field-emission scanning electron microscopy (SEM, Gemini 300). Transmission electron microscopy (TEM) images and high-resolution TEM (HRTEM) images were obtained by using JEM-F200 TEM. The crystalline phases of the as-prepared samples were analyzed by using D8 focus x-ray diffraction (XRD, Mini Flex 600, Bruker) with $\lambda = 1.5406$ Å Cu Kα irradiation. X-ray photoelectron spectroscopy (XPS, ESCALB MK-II, VG Instruments, UK) was employed to examine the chemical states of the samples, with C1s XPS peaks used for calibration for the binding energies. The vibrational bonds of the as-prepared samples were examined by Raman scattering (HR RamLab) using a 532 nm laser. Brunauer–Emmett–Teller (BET) method was employed to estimate the specific surface area of the as-prepared samples.

2.3. Electrochemical evaluation

The electrochemical measurements were conducted on a CHI760E potentiostat (CH Instruments Inc.) using a three-electrode system consisting of the Hg/HgO electrode, graphite rod, and electrocatalyst or commercial 20 wt% Pt/C (particle size is around 5 nm) coated glassy carbon electrode (GCE, 0.071 cm^2) as the reference, counter, and working electrodes, respectively. To prepare the working electrode, 10 mg ml^{-1} of the electrocatalyst or commercial 20 wt% Pt/C was placed and sonicated in 75% ethanol containing 0.5% Nafion (Dupont).

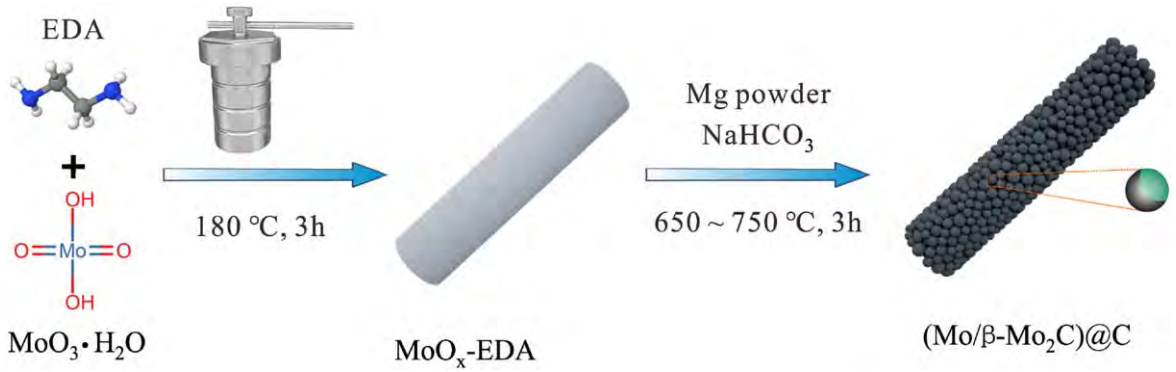

Figure 1. Schematic illustration of the synthesis of the hierarchical (Mo/β-Mo_2C)@C heterostructure.

10 μl of the ink was dropped onto the GCE and dried in air to form the working electrode. The catalyst or commercial loading was about 1.4 mg cm^{-2}. All the potentials were converted to the potentials referenced to the reversible hydrogen electrode (RHE) according to Nernst equation ($E_{(RHE)} = E_{(Hg/HgO)} + 0.098 + 0.059\ V \times pH$). The HER properties were studied by linear sweep voltammetry at a scanning rate of 5 mV s^{-1} in 1 M KOH (pH = 13.8) and 0.5 M H_2SO_4 (pH = 0.37), respectively. Electrochemical impedance spectroscopy (EIS) was carried out at −0.15 V in the frequency range between 100 kHz and 0.1 Hz with an AC perturbation of 5 mV. In the non-Faradic window, CV was conducted to determine the double-layer capacitance (C_{dl}) at different scanning rates (5–25 mV s^{-1}). The long-term stability was assessed by cyclic CV at a scanning rate of 100 mV s^{-1} between 0.05 and −0.15 V as well as chronoamperometry at a current density of 15 mA cm^{-2}. All the presented data were *iR* corrected.

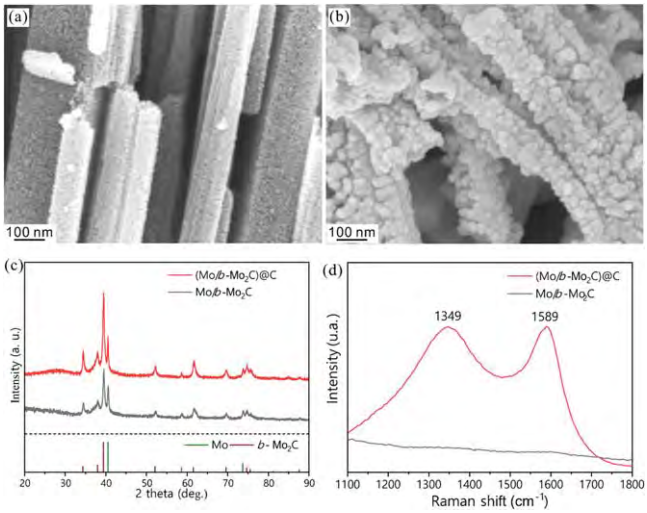

Figure 2. SEM images of (a) Mo/β-Mo_2C and (b) (Mo/β-Mo_2C)@C; (c) XRD patterns and (d) Raman scattering spectra of the Mo/β-Mo_2C and (Mo/β-Mo_2C)@C heterostructures.

3. Result and discussion

Synthesis of the Janus (Mo/β-Mo_2C)@C heterostructure is schematically illustrated in figure 1. The MoO_x-EDA nanorods are prepared by a hydrothermal process using $MoO_3 \cdot H_2O$ and EDA. As shown in figure S1, the prepared MoO_x-EDA has a nanorod-like morphology and low-temperature MTR is then conducted to produce the Janus (Mo/β-Mo_2C)@C heterostructure with the metal-metal carbide heterojunction encapsulated with carbon.

The pristine MoO_x-EDA was mixed with $NaHCO_3$ and magnesium powders and then treated at a temperature of 650, 700, and 750 °C for 3 h, respectively. Figure S2 shows the morphology and the crystal structure of the products. After the MTR treatment at 650 °C, the morphology remains almost unchanged, but the phase is transformed to MoOC (JCPDS Card no. 17–0104) as compared to that of MoO_x-EDA. The increase in reaction temperature to 700 °C provides a porous structure consisting of metallic molybdenum (JCPDS Card no. 42–1120) and β-Mo_2C (JCPDS Card no. 35–0787) (figure S2d). With an increase in the MTR temperature to 750 °C, the nanorod structure is broken and the main product is metallic molybdenum (figure S2d). Figure S3 compares the electrocatalytic HER activity (in 1 M KOH) of the MTR samples treated at different temperatures. The results show that the optimal temperature of MTR treatment is determined to be 700 °C, and the (Mo/β-Mo_2C)@C heterostructure is fabricated at this optimum temperature as will be discussed later.

As shown in figures 2(a)–(b), the heterostructured Mo/β-Mo_2C and (Mo/β-Mo_2C)@C samples are prepared using the MoO_x-EDA nanorods as precursors. The former is prepared by calcination at 750 °C for 3 h under H_2/Ar (figure 2(a)), whereas the latter is fabricated by a magnesium thermic process at 700 °C for 3 h (figure 2(b)). During the magnesium thermic process, Mg, MgO, Mo, and β-Mo_2C are produced (figure S4) via reduction of MoO_x-EDA to metallic Mo and β-Mo_2C which facilitate formation of the heterojunctions by possible metal and metal carbide (metal-metal carbide) interactions. Moreover, $NaHCO_3$ thermally decomposes at 400°C–500°C to release CO_2 that further reacts with Mg to form carbon leading to the formation of the Mo/β-Mo_2C heterostructure encapsulated with carbon ((Mo/β-Mo_2C)@C) with a larger surface area. To verify the proposed formation mechanism of the hierarchical (Mo/β-Mo_2C)@C, control experiments (Mg + MoO_x-EDA, Mg + $NaHCO_3$) are conducted. As shown in figures S5 and S6, the products after Mg + MoO_x-EDA reacting at 700 °C for 3 h

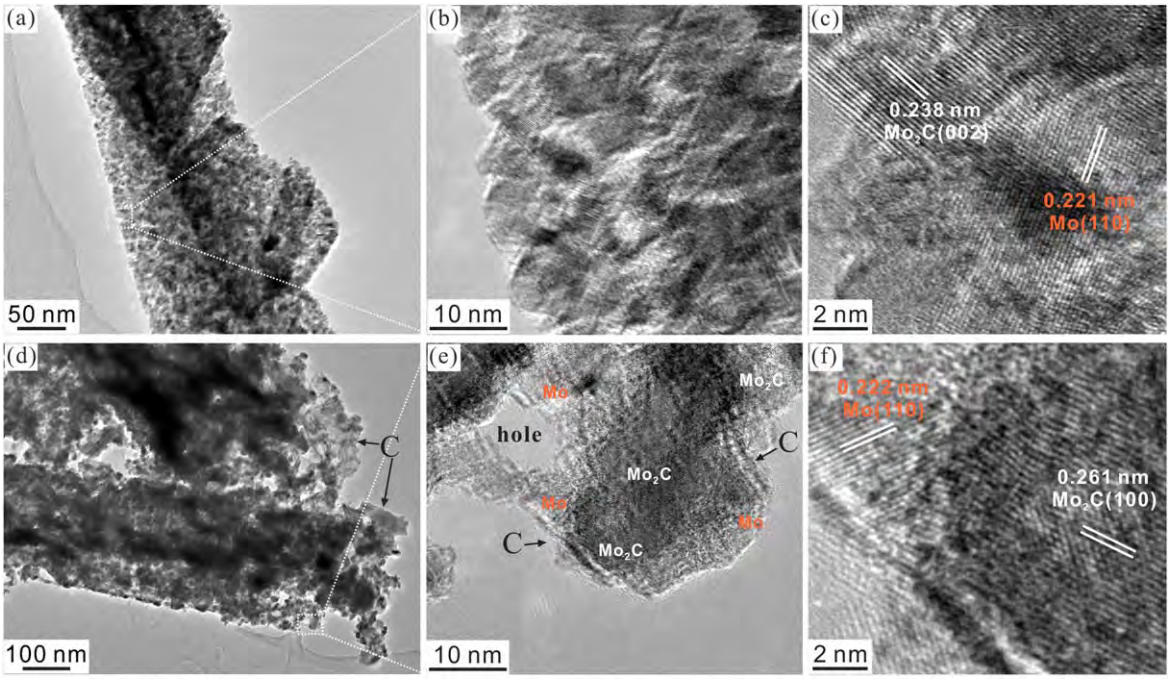

Figure 3. TEM and HR-TEM images of Mo/β-Mo_2C (a)–(c) and Mo/β-Mo_2C@C (d)–(e).

without rinsing are MgO, Mo, and β-Mo_2C (XRD pattern) with a negligible amount of carbon (Raman spectra). Carbon species are formed after rinsing the Mg and $NaHCO_3$ reaction (figure S6). In addition, we also investigated the effect of the ratios of MoO_x-EDA : Mg on the structures of (Mo/β-Mo_2C)@C. As shown in figures S7(a)–(c), the morphology of the samples changes with the MoO_x-EDA and Mg mass ratio and the rod-like structure deteriorates with increasing Mg.

The crystal structure is examined by XRD. The peaks at 40.5°, 58.6°, and 73.7° correspond to the (110), (200), and (211) facets of metallic molybdenum (JCPDS Card no. 42–1120) arising from excess metallic molybdenum (figure 2(c)). The amount of metallic molybdenum (Mo) is positively related with the Mg mass ratio. As shown in figure S7(d), the peaks corresponding to metallic molybdenum changes with the ratio of MoO_x-EDA to Mg and the optimal ratio is 2:1 which will be discussed further later. The other peaks at 34.3°, 37.9°, 39.3°, 52.1°, 61.5°, 69.5°, 72.3°, 74.6°, and 75.5° stems from the (100), (002), (101), (102), (110), (103), (200), (112), and (201) planes of β-Mo_2C (JCPDS Card no. 35–0787), respectively. Moreover, the Raman scattering results are presented in figure 2(d). In the (Mo/β-Mo_2C)@C heterostructure, the peaks at 1,349 and 1,589 cm^{-1} represent the disordered (D) band and graphitic (G) band of carbon [35], respectively, confirming the successful encapsulation of the catalyst by carbon as will be discussed later. However, those peaks are hardly observed from the Mo/β-Mo_2C heterostructure.

TEM is conducted to observe the structure of Mo/β-Mo_2C and (Mo/β-Mo_2C)@C. As shown in figures 3(a)–(b), the surface of Mo/β-Mo_2C is smooth, and the particles are closely packed with no obvious channels and pores within the structure. The lattice fringes of 0.221 and 0.238 nm in the high-resolution TEM (HR-TEM) image (figure 3(c)) are corresponding to the (110) and (002) crystal planes of metallic molybdenum and Mo_2C, respectively, in line with the XRD analysis. As shown in figure 3(d), (Mo/β-Mo_2C)@C has a porous networked structure with small nanoparticles between 10 and 30 nm in size embedded in the carbon layer. The large-magnification TEM image (figures S8 and 3(e)) clearly shows the (Mo/β-Mo_2C)@C catalyst has an inter-connected nanoparticles associated with the carbon network. The HR-TEM image (figure 3(f)) shows the Janus structure with nanopores of the (Mo/β-Mo_2C)@C. The lattice fringe of 0.220 nm corresponds to the (110) plane of metallic Mo and the interplanar spacings of 0.261 nm and 0.240 nm are indexed to the (110) and (002) planes of Mo_2C consistent with XRD result. The metal-metal carbide heterojunction at the interface of Mo and β-Mo_2C is expected to create active sites for electrocatalytic hydrogen evolution. The carbon layer not only improves electron transport, but also bodes well for prolonged operation by protecting Mo and β-Mo_2C NPs from dissolution and oxidation during the electrocatalytic reaction [39].

XPS is carried out to determine the chemical composition and chemical states of Mo/β-Mo_2C and (Mo/β-Mo_2C)@C (figure 4), which showed similar peaks for both samples. The six deconvoluted peaks of Mo 3d in figure 4(a) indicate the three oxidation states of Mo°, Mo^{+2}, and Mo^{+4} and those at 227.7 and 230.9 eV arise from metallic molybdenum [40]. The deconvoluted peaks of Mo^{+4} and Mo^{+2} stem from MoO_2 from air exposure and Mo_2C [41, 42], respectively. As shown in figure 4(b), the peaks at 284.8 and 283.3 eV arise from C–C and Mo–C bonds [40, 43], respectively.

The HER characteristics of (Mo/β-Mo_2C)@C are determined in both alkaline and acidic media with a deposition amount of 1.4 mg cm^{-2} on the GCE. The electrocatalytic

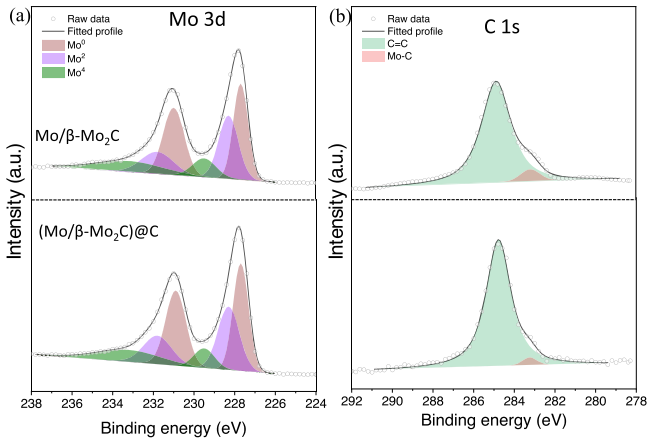

Figure 4. XPS spectra of (a) Mo 3d and (b) C1s (up: Mo/β-Mo_2C, down: (Mo/β-Mo_2C)@C).

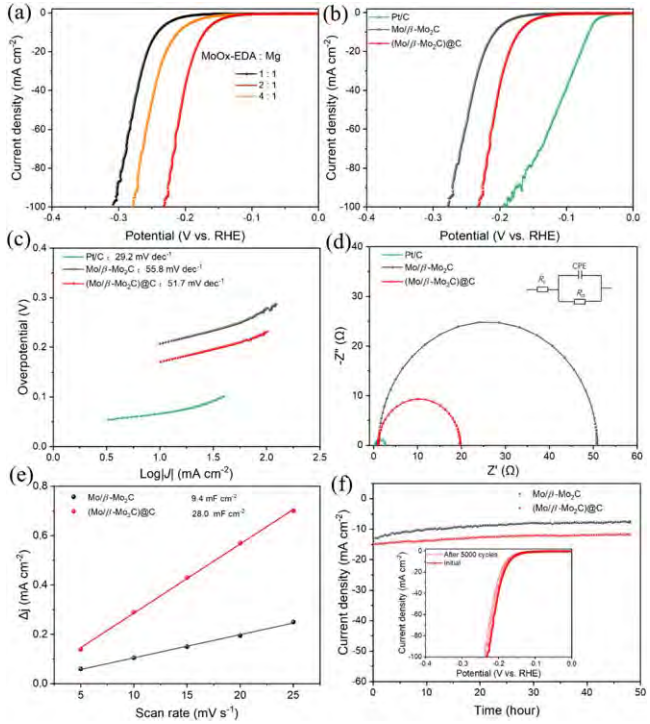

Figure 5. (a) Polarization curves of the samples synthesized using MoO_x-EDA : Mg ratios from 1:1 to 4:1; (b) Polarization curves and (c) Tafel plots of Mo/β-Mo_2C, (Mo/β-Mo_2C)@C, and commercial Pt/C in 1 M KOH; (d) Nyquist plots of Mo/β-Mo_2C, (Mo/β-Mo_2C)@C, and commercial Pt/C at −150 mV with inset showing the electrical equivalent circuit; (e) Estimation of C_{dl} by plotting the current density variation at 0.2 V versus RHE against scanning rates to obtain linear fits; (f) Stability evaluation of Mo/β-Mo_2C and (Mo/β-Mo_2C)@C showing the chronoamperometric curves at a current density of 15 mA cm^{-2} with the inset showing the initial and 5000th cycle polarization curves of (Mo/β-Mo_2C)@C.

HER properties are first investigated in a 1 M KOH solution. Figure 5(a) shows the polarization curves of the (Mo/β-Mo_2C)@C fabricated with MoO_x-EDA to Mg ratios varied from 1:1 to 4:1 and the best performance is achieved with a MoO_x-EDA:Mg ratio of 2:1. The properties of Mo/β-Mo_2C and commercial 20 wt% Pt/C are also compared with the same loading amount. As shown in figure 5(b), Pt/C has good HER properties especially at low current densities, whereas the HER current density of (Mo/β-Mo_2C)@C increases rapidly at more negative potentials. In addition, (Mo/β-Mo_2C)@C has better HER activity than Mo/β-Mo_2C. In particular, (Mo/β-Mo_2C)@C shows current densities of 1 and 10 mA cm^{-2} at low overpotentials of 66 (η_1) and 171 mV (η_{10}), whereas η_1 and η_{10} of Mo/β-Mo_2C are 149 and 207 mV, respectively, indicating faster hydrogen formation on (Mo/β-Mo_2C)@C. The corresponding Tafel slopes obtained from the polarization curves of (Mo/β-Mo_2C)@C and Mo/β-Mo_2C are 51.7 and 55.8 mV dec^{-1}, which are less than 120 mV dec^{-1} (figure 5(c)) suggesting the Volmer–Heyrovsky mechanism [44] with better HER kinetics on (Mo/β-Mo_2C)@C. EIS measurement is employed to elucidate the mechanism at the electrode/electrolyte interface. As shown by the Nyquist plots in figure 5(d), the semicircle diameter observed from (Mo/$\beta\beta$-Mo_2C)@C is smaller than that of Mo/β-Mo_2C, indicating the fast electron transfer at the electrode/electrolyte interface [45]. The smaller charge transfer resistance (R_{ct}) obtained from the (Mo/β-Mo_2C)@C is due to the encapsulated carbon layer that improves the conductivity and electron transport [29, 36]. The equivalent circuit employed for data fitting is indicated in the inset of figure 5(d), where R_{ct} denotes the barrier that electrons must cross to combine with the electroactive species adsorbed on the surface of the electrode.

The better electrocatalytic activity of the Janus (Mo/β-Mo_2C)@C nanostructure may stem from the larger electrochemical active surface area which is directly related to the electrochemical double-layer capacity (C_{dl}). Therefore, C_{dl} is estimated by CV conducted at different scanning rates (figure S8). The C_{dl} value of (Mo/β-Mo_2C)@C is 28.0 mF cm^{-2}, which is about 3 times larger than that of Mo/β-Mo_2C (9.4 mF cm^{-2}) (figure 5(e)), confirming that the magnesium thermic reaction increases the surface roughness as showed by SEM (figures 2(a)–(b)). This is further confirmed by the specific surface areas (S_{BET}) of the Mo/β-Mo_2C and (Mo/β-Mo_2C)@C using the BET method (figure S9). (Mo/β-Mo_2C)@C has a larger S_{BET} of 78.4 m^2 g^{-1} compared to the 59.3 m^2 g^{-1} of Mo/β-Mo_2C. The large specific surface area of the (Mo/β-Mo_2C)@C catalyst stems from a large amount of exposed active sites due to the successful encapsulation with the carbon layer that eventually results in an excellent HER catalytic activity [46]. Because the emerged porous network in the encapsulated catalyst allows an increased exposure of active site and thus, surges the HER activity[47]. In addition, the encapsulation, of the closely attached carbons, could also contribute to HER activity due to their better conductivity which enables fast electron transfer [36]. Long-term electrolysis is carried out by chronoamperometry. at 15 mA cm^{-2} for 48 h and negligible deactivation is observed from (Mo/β-Mo_2C)@C (figure 5(f)). Similarly, as shown in the inset in figure 5(f), the polarization curve of (Mo/β-Mo_2C)@C obtained after 5000 cycles is almost the same as the initial one and the SEM and XRD result in figures S10 and S11 reveal no noticeable change in the morphology and crystal structure after chronoamperometry. In addition, the durability of the (Mo/β-Mo_2C)@C catalyst is

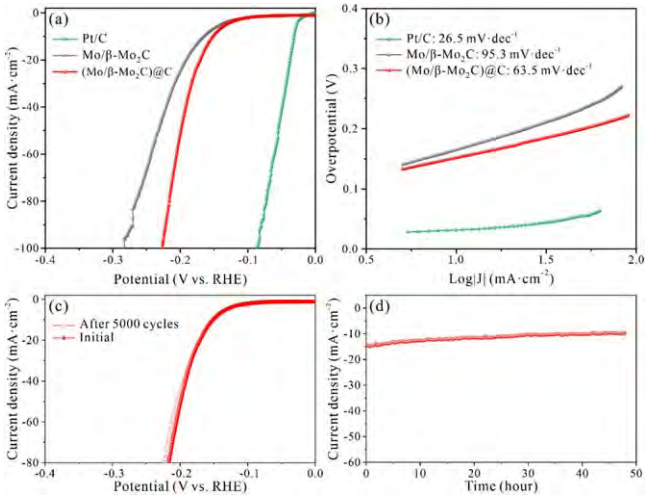

Figure 6. (a) Polarization curves and (b) Tafel plots of Mo/β-Mo_2C, (Mo/β-Mo_2C)@C, and commercial Pt/C obtained in 0.5 M H_2SO_4; stability evaluation of (Mo/β-Mo_2C)@C: (c) initial polarization curve and that after 5000 cycles and (d) chronoamperometric curve at a current density of 15 mA cm^{-2}.

investigated at a large current density of ~100 mA cm^{-2} and the plot shows excellent stability up to 48 h (figure S12). The TEM images of the sample after the HER stability test reveal no apparent changes (figure S13). The outstanding stability is realized due to the encapsulation of the catalyst with carbon which improves the presence of active sites for HER. Therefore, encapsulation of the catalyst not only enables to boost the HER activity but also improves the long-time electrolysis.

In the second step, the HER catalytic activity of Mo/β-Mo_2C and (Mo/β-Mo_2C)@C is evaluated in 0.5 M H_2SO_4. Similar to the performances obtained in the alkaline solution discussed above, the Janus (Mo/β-Mo_2C)@C composite shows higher catalytic activity in the acidic electrolyte than Mo/β-Mo_2C (figure 6(a)). The Tafel slopes of (Mo/β-Mo_2C)@C and Mo/β-Mo_2C are 63.5 mV dec^{-1} and 95.3 mV dec^{-1}, respectively, suggesting faster electrocatalytic HER kinetics on (Mo/β-Mo_2C)@C [48]. (Mo/β-Mo_2C)@C also shows outstanding long-term stability in 0.5 M H_2SO_4 as evidenced by the negligible decline in the activity after chronoamperometry for 5000 cycles and 48 h (figures 6(c)–(d)). Similar to the alkaline conditions, the (Mo/β-Mo_2C)@C catalyst shows reasonable durability at large current density (~100 mA cm^{-2}) in acidic electrolyte for 48 h (figure S14), suggesting the importance of encapsulation for long-term operation in both acidic and alkaline media.

4. Conclusion

The metal-metal carbide Mo/β-Mo_2C and (Mo/β-Mo_2C)@C heterojunctions are synthesized and the HER properties are determined in both acidic and alkaline media. Promoting from the greater conductivity and fast electron transport of the carbon layer, and the metal-metal carbide active interfaces, the prepared (Mo/β-Mo_2C)@C heterojunction shows better HER activity in both alkaline and acidic media. The low overpotentials recorded from (Mo/β-Mo_2C)@C are 152 and 171 mV at a current density of 10 mA cm^{-2} and small Tafel slopes of 51.7 and 63.5 mV dec^{-1} in acidic and alkaline media, respectively. The (Mo/β-Mo_2C)@C heterojunction exhibits not only outstanding HER activity but also long-term durability in both acidic and alkaline electrolytes. Because the encapsulating carbon layer prevents the active sites from corrosion and oxidation leading to better stability and durability. The materials and design have large potential in the development of high-performance noble-metal-free catalysts for water splitting and other applications.

Acknowledgments

This work was financially supported by Scientific Research Foundation of Shantou University (NTF21022), the Guangdong Basic and Applied Basic Research Foundation (2019A1515010076), 2020 Li Ka Shing Foundation Cross-Disciplinary Research Grant (2020LKSFG01A , 2020LKSFG09A), and City University of Hong Kong Donation Research Grant (DON-RMG 9229021).

Data availability statement

All data that support the findings of this study are included within the article (and any supplementary files).

Supplementary data

Supplementary material related to this article can be found in the online version at doi:

ORCID iDs

Abebe Reda Woldu https://orcid.org/0000-0002-8927-1602
Fushen Lu https://orcid.org/0000-0002-3323-7181
Liangsheng Hu https://orcid.org/0000-0002-4133-2090

References

[1] Sullivan I, Goryachev A, Digdaya I A, Li X, Atwater H A, Vermaas D A and Xiang C 2021 Coupling electrochemical CO_2 conversion with CO_2 capture *Nat. Catal.* **4** 952–8
[2] Woldu A R, Huang Z, Zhao P, Hu L and Astruc D 2022 Electrochemical CO_2 reduction (CO_2RR) to multi-carbon products over copper-based catalysts *Coordin. Chem. Rev.* **454** 214340
[3] Akbar M B, Gong Y, Wang Y, Woldu A R, Zhang X and He T 2021 Role of TiO_2 coating layer on the performance of Cu_2O photocathode in photoelectrochemical CO_2 reduction *Nanotechnology* **32** 395707
[4] Shah A H, Wang Y, Hussain S, Akbar M B, Woldu A R, Zhang X and He T 2020 New aspects of C_2 selectivity in electrochemical CO_2 reduction over oxide-derived copper *Phys. Chem. Chem. Phys.* **22** 2046–53

[5] Woldu A R 2020 From low to high-index facets of noble metal nanocrystals: a way forward to enhance the performance of electrochemical CO_2 reduction *Nanoscale* **12** 8626–35

[6] Zhu J, Hu L, Zhao P, Lee L Y S and Wong K-Y 2019 Recent advances in electrocatalytic hydrogen evolution using nanoparticles *Chem. Rev.* **120** 851–918

[7] Rafiq M, Hu X, Ye Z, Qayum A, Xia H, Hu L, Lu F and Chu P K 2022 Recent advances in structural engineering of 2D hexagonal boron nitride electrocatalysts *Nano Energy* **91** 106661

[8] Hu L, Li Y, Peng X, Zheng W, Xu W, Zhu J, Lee L Y S, Chu P K and Wong K-Y 2021 TiO_2 film supported by vertically aligned gold nanorod superlattice array for enhanced photocatalytic hydrogen evolution *Chem. Eng. J.* **417** 127900

[9] Wang Z, Wang P, Mao Q, Tian W, Xu Y, Li X, Wang L and Wang H 2022 Urchin-like PdOs nanostructure for hydrogen evolution electrocatalysis *Nanotechnology* **33** 325401

[10] Peng X, Yan Y, Xiong S, Miao Y, Wen J, Liu Z, Gao B, Hu L and Chu P K 2022 Se-$NiSe_2$ hybrid nanosheet arrays with self-regulated elemental Se for efficient alkaline water splitting *J. Mater. Sci. Technol.* **118** 136–43

[11] Qayum A *et al* 2022 Highly Durable and Efficient Ni-FeO_x/$FeNi_3$ Electrocatalysts Synthesized by a Facile *In Situ* Combustion-Based Method for Overall Water Splitting with Large Current Densities *ACS Appl. Mater. Interfaces* **14** 27842–53

[12] Zhang J, Woldu A R, Peng X, Song Y, Xia H, Lu F, Chu P K and Hu L 2022 Plasmon-enhanced hydrogen evolution on Pt-anchored titanium nitride nanowire arrays *Appl. Surf. Sci.* **598** 153745

[13] Liu J-T, Hu L-S, Liu Y-L, Chen R-S, Cheng Z, Chen S-J, Amatore C, Huang W-H and Huo K-F 2014 Real-time monitoring of auxin vesicular exocytotic efflux from single plant protoplasts by amperometry at microelectrodes decorated with nanowires *Angew. Chem. Int. Ed.* **53** 2643–7

[14] Wang X, Xu C, Jaroniec M, Zheng Y and Qiao S-Z 2019 Anomalous hydrogen evolution behavior in high-pH environment induced by locally generated hydronium ions *Nat. Commun.* **10** 4876

[15] Yu W, Huang H, Qin Y, Zhang D, Zhang Y, Liu K, Zhang Y, Lai J and Wang L 2022 The synergistic effect of pyrrolic-N and pyridinic-N with Pt under strong metal-support interaction to achieve high-performance alkaline hydrogen evolution *Adv. Energy Mater.* **12** 2200110

[16] Peng X, Hu L, Wang L, Zhang X, Fu J, Huo K, Lee L Y S, Wong K-Y and Chu P K 2016 Vanadium carbide nanoparticles encapsulated in graphitic carbon network nanosheets: a high-efficiency electrocatalyst for hydrogen evolution reaction *Nano Energy* **26** 603–9

[17] Popczun E J, McKone J R, Read C G, Biacchi A J, Wiltrout A M, Lewis N S and Schaak R E 2013 Nanostructured nickel phosphide as an electrocatalyst for the hydrogen evolution reaction *J. Am. Chem. Soc.* **135** 9267–70

[18] Popczun E J, Read C G, Roske C W, Lewis N S and Schaak R E 2014 Highly active electrocatalysis of the hydrogen evolution reaction by cobalt phosphide nanoparticles *Angew. Chem. Int. Ed.* **53** 5427–30

[19] Yu P, Wang F, Shifa T A, Zhan X, Lou X, Xia F and He J 2019 Earth abundant materials beyond transition metal dichalcogenides: a focus on electrocatalyzing hydrogen evolution reaction *Nano Energy* **58** 244–76

[20] Fu H Q *et al* 2022 Hydrogen spillover-bridged volmer/tafel processes enabling ampere-level current density alkaline hydrogen evolution reaction under low overpotential *J. Am. Chem. Soc.* **144** 6028–39

[21] Lin H, Liu N, Shi Z, Guo Y, Tang Y and Gao Q 2016 Cobalt-doping in molybdenum-carbide nanowires toward efficient electrocatalytic hydrogen evolution *Adv. Funct. Mater.* **26** 5590–8

[22] Baek D S, Lee J, Kim J and Joo S H 2022 Metastable phase-controlled synthesis of mesoporous molybdenum carbides for efficient alkaline hydrogen evolution *ACS Catal.* **12** 7415–26

[23] Vrubel H and Hu X 2012 Molybdenum boride and carbide catalyze hydrogen evolution in both acidic and basic solutions *Angew. Chem. Int. Ed.* **51** 12703–6

[24] Xiao P, Ge X, Wang H, Liu Z, Fisher A and Wang X 2015 Novel molybdenum carbide–tungsten carbide composite nanowires and their electrochemical activation for efficient and stable hydrogen evolution *Adv. Funct. Mater.* **25** 1520–6

[25] Liao L, Wang S, Xiao J, Bian X, Zhang Y, Scanlon M D, Hu X, Tang Y, Liu B and Girault H H 2014 A nanoporous molybdenum carbide nanowire as an electrocatalyst for hydrogen evolution reaction *Energ. Environ. Sci.* **7** 387–92

[26] Wu C and Li J 2017 Unique hierarchical Mo_2C/C nanosheet hybrids as active electrocatalyst for hydrogen evolution reaction *ACS Appl. Mater. Interfaces* **9** 41314–22

[27] Wang H, Cao Y, Sun C, Zou G, Huang J, Kuai X, Zhao J and Gao L 2017 Strongly coupled molybdenum carbide on carbon sheets as a bifunctional electrocatalyst for overall water splitting *ChemSusChem* **10** 3540–6

[28] Ouyang T, Chen A-N, He Z-Z, Liu Z-Q and Tong Y 2018 Rational design of atomically dispersed nickel active sites in β-Mo_2C for the hydrogen evolution reaction at all pH values *Chem. Commun.* **54** 9901–4

[29] Li F, Chen L, Liu H, Wang D, Shi C and Pan H 2019 Enhanced N_2-fixation by engineering the edges of two-dimensional transition-metal disulfides *J. Phys. Chem.* C **123** 22221–7

[30] Wang J, Yan M, Zhao K, Liao X, Wang P, Pan X, Yang W and Mai L 2017 Field effect enhanced hydrogen evolution reaction of MoS_2 nanosheets *Adv. Mater.* **29** 1604464

[31] Hu Y, Yu B, Ramadoss M, Li W, Yang D, Wang B and Chen Y 2019 Scalable synthesis of heterogeneous W–W_2C nanoparticle-embedded CNT networks for boosted hydrogen evolution reaction in both acidic and alkaline media *ACS Sustain. Chem. Eng.* **7** 10016–24

[32] Wang P, Zhu J, Pu Z, Qin R, Zhang C, Chen D, Liu Q, Wu D, Li W and Liu S 2021 Interfacial engineering of Co nanoparticles/Co_2C nanowires boosts overall water splitting kinetics *Appl. Catal. B Environ.* **296** 120334

[33] Wei H, Wang J, Lin Q, Zou Y, Chen X A, Zhao H, Li J, Jin H, Lei Y and Wang S 2021 Incorporating ultra-small N-doped Mo_2C nanoparticles onto 3D N-doped flower-like carbon nanospheres for robust electrocatalytic hydrogen evolution *Nano Energy* **86** 106047

[34] Li Y *et al* 2019 Photocatalytic water splitting by N-TiO_2 on MgO (111) with exceptional quantum efficiencies at elevated temperatures *Nat. Commun.* **10** 1–9

[35] Wu Y-L, Li X, Wei Y-S, Fu Z, Wei W, Wu X-T, Zhu Q-L and Xu Q 2021 Ordered macroporous superstructure of nitrogen-doped nanoporous carbon implanted with ultrafine Ru nanoclusters for efficient pH-universal hydrogen evolution reaction *Adv. Mater.* **33** 2006965

[36] Wu R, Zhang J F, Shi Y M, Liu D and Zhang B 2015 Metallic WO_2-carbon mesoporous nanowires as highly efficient electrocatalysts for hydrogen evolution reaction *J. Am. Chem. Soc.* **137** 6983–6

[37] Zhang J, Ji Y, Wang P, Shao Q, Li Y and Huang X 2020 Adsorbing and Activating N_2 on Heterogeneous Au–Fe_3O_4 Nanoparticles for N_2 Fixation *Adv. Funct. Mater.* **30** 1906579

[38] Huang Z, Zhao X, Xia H, Lu F, Hu L and Chu P K 2021 Insights into enhancement of photocatalytic properties of g-C_3N_4 by local electric field induced by polarization of MgO(111) *J. Environ. Chem, Eng.* **9** 105922

[39] Chen C, Yan D, Wang Y, Zhou Y, Zou Y, Li Y and Wang S 2019 B-N pairs enriched defective carbon nanosheets for ammonia synthesis with high efficiency *Small* **15** 1805029
[40] Reynard D, Nagar B and Girault H 2021 Photonic flash synthesis of Mo_2C/graphene electrocatalyst for the hydrogen evolution reaction *ACS Catal.* **11** 5865–72
[41] Jiang J, Liu Q, Zeng C and Ai L 2017 Cobalt/molybdenum carbide@ N-doped carbon as a bifunctional electrocatalyst for hydrogen and oxygen evolution reactions *J. Mater. Chem.* A **5** 16929–35
[42] Guo J, Wang J, Wu Z, Lei W, Zhu J, Xia K and Wang D 2017 Controllable synthesis of molybdenum-based electrocatalysts for a hydrogen evolution reaction *J. Mater. Chem.* A **5** 4879–85
[43] Xiong J *et al* 2018 *In situ* engineering of double-phase interface in Mo/Mo_2C heteronanosheets for boosted hydrogen evolution reaction *ACS Energy Lett.* **3** 341–8
[44] Tian J, Liu Q, Asiri A M and Sun X 2014 Self-supported nanoporous cobalt phosphide nanowire arrays: an efficient 3D hydrogen-evolving cathode over the wide range of pH 0–14 *J. Am. Chem. Soc.* **136** 7587–90
[45] Defeng Q *et al* 2022 High-efficiency electrocatalytic NO reduction to NH_3 by nanoporous VN *Nano Res. Energy* **1** e9120022
[46] Pu Z, Amiinu I S, Wang M, Yang Y and Mu S 2016 Semimetallic MoP_2: an active and stable hydrogen evolution electrocatalyst over the whole pH range *Nanoscale* **8** 8500–4
[47] Liu Y, Zhang X, Zhang W, Ge X, Wang Y, Zou X, Zhou X and Zheng W 2022 MXene-based quantum dots optimize hydrogen production via spontaneous evolution of Cl- to O-terminated surface groups *Energy Environ. Mater.* e12438
[48] Zhang H, Luo Y, Chu P K, Liu Q, Liu X, Zhang S, Luo J, Wang X and Hu G 2022 Recent advances in non-noble metal-based bifunctional electrocatalysts for overall seawater splitting *J. Alloys Compd.* **922** 166113